

Article

# Study on the Flame Transition Characteristics of a Gas Turbine Combustor

Mingmin Chen <sup>1</sup>, Li Wang <sup>2</sup>, Xinbo Huang <sup>1</sup>, Minwei Zhao <sup>1</sup>, Lingwei Zeng <sup>3</sup>, Hongtao Zheng <sup>1</sup> and Fuquan Deng <sup>1,3,\*</sup>

<sup>1</sup> College of Power and Energy Engineering, Harbin Engineering University, Harbin 150001, China; chenmm2@shanghai-electric.com (M.C.); 15895672761@163.com (X.H.); zhaominwei@hrbeu.edu.cn (M.Z.); zhenghongtao9000@163.com (H.Z.)

<sup>2</sup> Shanghai Marine Diesel Engine Research Institute, Shanghai 200237, China; 57819501@163.com

<sup>3</sup> Department of Mechanical Engineering, The Hong Kong Polytechnic University, Hong Kong SAR 999077, China; lingwei.zeng@connect.polyu.hk

\* Correspondence: adsdengfuquan@hrbeu.edu.cn

**Abstract:** Gas turbines are widely used as important equipment for electricity generation on islands and offshore platforms. During the operation of a gas turbine, the flame shape in the combustion chamber undergoes variations in response to changes in parameters such as gas turbine load, fuel distribution, and burner structure. These alterations in flame shape exert influence on combustion instability, emissions, and load characteristics. This study explores the variations in flame transition, emissions, and operating parameters among three distinct center stage structures: namely, the non-premix center stage (NPCS), premix center stage (PCS), and enhanced premix center stage (PCSE). The investigation is conducted using a heavy-duty gas turbine hybrid burner on a full temperature, full pressure, and full-size single burner experimental bench. Simultaneously, a multi-parameter numerical simulation regarding the influence of the central fuel split on flame shape analysis was conducted using the PCS burner under the design point for a more in-depth understanding of the mechanisms and for influencing factors associated with flame transition. The findings indicate that variations in flame transition loads among different central stage structures: for the NPCS burner, the transition occurs between 45% and 50% load; for the PCS burners, it takes place between 60% and 65% load; for the PCSE burners, it shifts between 55% and 60% load. Additionally, a reduction in NO<sub>x</sub> emissions is observed during the flame transition process. Furthermore, it was found that decreasing the central stage fuel results in a decline in flame angle for the same burner structure. As the central stage fuel diminishes to a specific value, the flame shape undergoes a sudden change. Further reduction in central stage fuel does not significantly affect the flame shape and temperature distribution.

**Keywords:** gas turbine; premix combustion; flame transition; NO<sub>x</sub>; center stage structure



**Citation:** Chen, M.; Wang, L.; Huang, X.; Zhao, M.; Zeng, L.; Zheng, H.; Deng, F. Study on the Flame Transition Characteristics of a Gas Turbine Combustor. *J. Mar. Sci. Eng.* **2024**, *12*, 719. <https://doi.org/10.3390/jmse12050719>

Academic Editor: Dejan Brkić

Received: 10 March 2024

Revised: 13 April 2024

Accepted: 23 April 2024

Published: 26 April 2024



**Copyright:** © 2024 by the authors. Licensee MDPI, Basel, Switzerland. This article is an open access article distributed under the terms and conditions of the Creative Commons Attribution (CC BY) license (<https://creativecommons.org/licenses/by/4.0/>).

## 1. Introduction

Due to the high cost of electricity transmission infrastructure with the mainland, the electricity of islands cannot be obtained from the mainland, which requires islands to generate their own electricity [1]. Gas turbines, as one of the important power sources for island power plants [2], have the advantages of high efficiency, high pressure ratio, and low pollution [3], and the current modular structure of gas turbines is easy to be transported and maintained [4], which makes it suitable for constructing power plants on the limited land on islands. Offshore platforms have a very high demand for electricity [5] and usually use gas turbines to generate electricity. Gas turbine electricity generation has the advantages of high flexibility and small size [6], and the natural gas extracted from offshore platforms can be used as the fuel for electricity generation, which saves the transportation cost of fuel. The application of gas turbines in island and offshore platform electricity generation is promising and has attracted wide attention.

Most Aegean island electric power plants use gas turbines almost exclusively as power units [1]. Lv et al. [7] also proposed a gas turbine island energy system burning biomass gas with an electrical efficiency of 60.78%. With the continuous advancement of advanced, efficient, and clean gas turbine combustion technologies [8], coupled with increasingly stringent emission regulations [9,10], the development of the gas turbine encounters new challenges and demands, including the imperative to simultaneously achieve for higher efficiency, lower NO<sub>x</sub> and CO emissions, greater fuel flexibility, and a larger operation window [11,12]. The wider operation window is characterized by lower park loads [13], indicating the operational state of the gas turbine at lower loads, and higher ramp gradients, denoting a greater rate of change when adjusting the load, which showcases the greater flexibility and adaptability of gas turbines various operational conditions [14–16]. Specifically, increasing the equivalence ratio to enhance combustion is very effective in extending the operation window. Nevertheless, this results in a trade-off—an increase in NO<sub>x</sub> emissions, posing challenges to the goal of achieving lower emissions. Consequently, it can be concluded that addressing the challenge of extending the operational window for the heavy-duty gas turbine combustor while simultaneously ensuring stability, efficiency, and environmental friendliness is crucial.

Traditional combustion chambers commonly utilize diffusive combustion technology [17]. Despite demonstrating great operational stability, these chambers encounter elevated temperatures in the primary combustion zone, leading to an increase in pollutant emissions. The fundamental strategy for controlling NO<sub>x</sub> generation involves maintaining a lean equivalence ratio in the combustion zone and ensuring uniformity in the local equivalence ratio across all operating conditions [18]. In light of this, some gas turbine original equipment manufacturers (OEMs) develop lean premix combustion technology and multi-stage combustion to enlarge the operation window while simultaneously minimizing NO<sub>x</sub> emission. As shown in Figure 1, the combustion chamber of heavy-duty gas turbine developed by Siemens [19] is an annular combustor, featuring a coaxial center-staged burner configuration, with the pilot stage located at the center and the main stage in the outer [20,21]. This design is widely used in SIEMENS's F class gas turbine and is also performed in a lot of experimental tests [22,23]. The pilot stage primarily serves to stabilize the combustion through diffusion combustion and a higher fuel concentration. In contrast, the main stage is designed to achieve lower NO<sub>x</sub> emissions through lean premix combustion [24]. General Electric developed an advanced Dry Low NO<sub>x</sub> (DLN) combustion system for their heavy-duty gas turbine, which utilizes the multi-nozzle combustion approach strategically arranged in the combustion chamber to optimize combustion efficiency and reduce NO<sub>x</sub> emissions in their can-annular system [25–27]. Another typical stage fuel combustion system is the GT24/GT26 heavy-duty gas turbines sequential combustion system proposed by Alstom [28,29]. This system features an axial stage combustion design, with the first stage utilizing a premix mode and the second stage integrating a rehear combustor [30,31]. The sequential combustion technology improves both operability and fuel flexibility of gas turbines, consequently facilitating stable combustion and minimizing emissions across a broad range of engine loads [32,33]. For H-Class gas turbines, General Electric has innovated a new-generation Dry Low NO<sub>x</sub> (DLN) system by using axial stages [34], which improves overall performance, ensures stable combustion, enhances operability, fuel capability, reliability, and facilitates the maintenance of low emissions [35]. In the development of the SGT5-8000H by Siemens [36], axial stages and multi-nozzles are also employed. Alstom proposed the GT36 as an evolution from the GT26, maintaining the two-stage combustion system, in which the first stage features a multi-nozzle with a new BEV burner, and the sequential combustor incorporates some new technologies [37].

During the development of Ansaldo Energia's coaxial multi-stage lean premix burner, an obvious sudden change in flame shape occurs during loading, and an inverse sudden change takes place during deloading, which is recognized as "flame transition" or "flame switch" [16,38]. As depicted in Figure 2, the left side shows the flame image before the flame transition at the end of the flame chamber during the test, while the right side

illustrates the flame image after the flame transition from the same perspective. Before the flame transition, the first and second row ceramic tiles near the burner outlet are brighter, indicating a higher temperature in this region. After the flame transition, the color of the first and second row ceramic tiles turns crimson, indicating a lower temperature. Additionally, the trails of the pilot flame in the left image are open, whereas they are closed and slightly rolled around the chamber centerline in the right image. Rofi et al. [16,38] employed both experiments and Reynolds Averaged Navier–Stokes (RANS) simulations to explore the flame shape before and after flame transition in a single burner combustion chamber developed by Ansaldo Energia. Their findings revealed distinctive flame shape transitions during load ramps, providing valuable insights into the dynamics of combustion stability and emission characteristics of their gas turbine combustor.

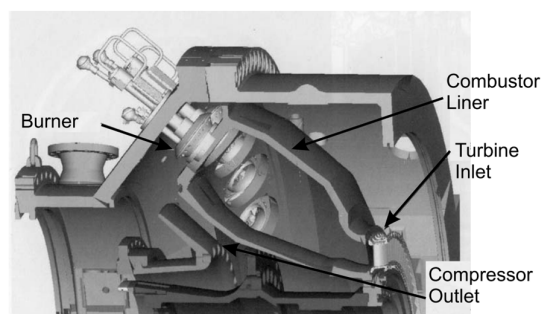


**Figure 1.** The annular combustor utilized in heavy duty gas turbine annular combustor developed by Siemens [19].

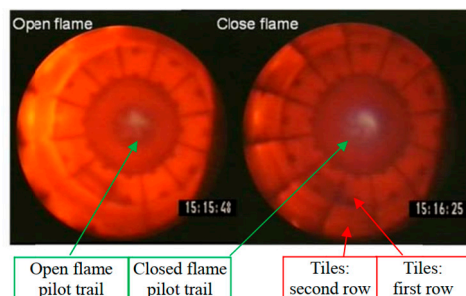


**Figure 2.** Open flame and closed flame configuration [38].

The phenomena associated with flame transitions are crucial yet intricate. To reveal the underlying mechanism and influencing factors of flame transition, this article examined the flame transition characteristics of three different central stage structures using a full temperature and full pressure single burner experimental bench under different operating parameters. During the experiment, the changes in flame shape were determined by monitoring the temperature and pressure distribution along the flame tube near the wall. Additionally, the influence of fuel distribution in the premixed central stage on flame morphology was analyzed through Computational Fluid Dynamics (CFD) calculations for the PCS burner.

## 2. Experimental

### 2.1. Full-Scale High-Pressure Test Rig

The configuration of the full-pressure, full-temperature, and full-size signal combustor used in this study is shown in Figure 3. The test rig includes an air system, pressure casing, combustion chamber, and so on. The test rig body features a dual-casing design, with the outer casing serving as the primary pressure-bearing component and the inner casing being designated for combustion. Ceramic tiles are arranged on the inner side to provide thermal

protection, and cooling air is present between the inner and outer casings to cool the metal and tile holders.

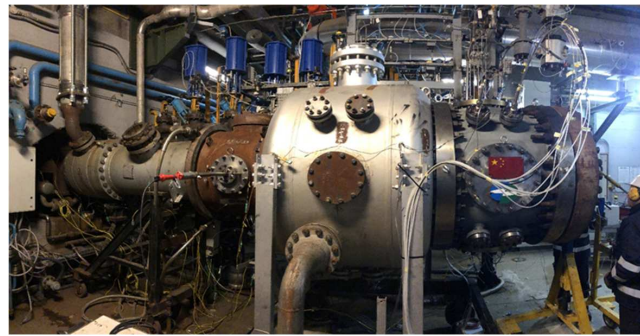


**Figure 3.** Test rig configuration.

## 2.2. Combustor

Figure 4 depicts the general burner configuration used in this study. The burner consists of a central stage positioned at the center and a main premix stage located at the periphery. Most of the air and fuel enter the combustion chamber through the main premix stage for combustion. Both the central stage and the main premix stage contain a swirler, with the central stage swirler being an axial swirler and the main premixed stage swirler being diagonal. An orifice plate is installed upstream of the central stage to adjust the air flow area in the central stage. In the main premix stage, air enters the burner upstream of the diagonal swirler blade, while the fuel enters the fuel cavity through the pipeline and is then injected from the holes on the blade, forming a transverse jet to enhance the mixing. For the central stage, air enters through the annular gap formed by the orifice plate and the peripheral circular tube before entering the channel of the swirl blade. There are two different injection modes for the central stage fuel. One is injected from the pipe between the swirler blades (Figure 5a) and is aligned with the direction of airflow to prevent the formation of a transverse jet, resulting in a poor mixing effect. This mode is referred to as non-premix central stage (NPCS). Another injection mode involves fuel injection from the holes on the axial swirler blade (Figure 5b), directed perpendicular to the incoming airflow, which forms a transverse jet to enhance mixing. This model is called the premix central stage (PCS). A modified injection mode, premix central stage enhanced (PCSE), is similar to PCS, but without the orifice plate to increase the air into the central stage so as to improve the mix quality between the fuel and the air. This article explores the influence of central stage combustion mode and fuel split between the main stage and the central stage on the flame transition by testing three different configurations (NPCS, PCS, and PCSE). The fuel used in the test is natural gas.

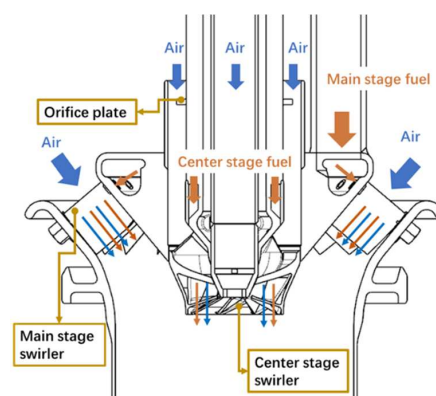


**Figure 4.** Burner configuration.

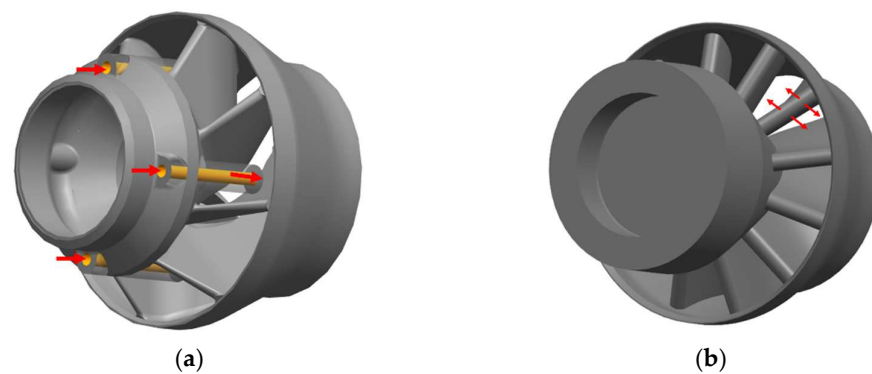


**Figure 5.** Central stage injection mode: (a) NPCS; (b) PCS.

### 2.3. Measurement Apparatus

This study mainly measures the experimental measurement data of static pressure, temperature, and  $\text{NO}_x$  emissions. The K-type thermocouples produced by DUCHIN Co., Ltd. (Chongqing, China) were used for the temperature measurement, featuring a wire diameter of 1.5 mm and a length of 5000 mm. Static pressure and differential pressure were measured using the PSI9216 pressure scanning valve produced by PSI company, supporting a maximum of 16 channels. To measure the temperature and pressure of hot gas inside the combustion chamber, K-type thermocouples and static pressure sensors are inserted deeply into the combustion chamber by drilling holes in its wall. There are 11 thermocouples and 10 differential pressure sensors along the axial direction of chamber, as shown in Figure 6. The 0 position corresponds to the combustion chamber inlet and serves as the reference point for differential pressure (defined as  $P_m - P_0$ , where  $m$  denotes the position of the pressure sensor and 0 means the reference position). A flue gas analyzer is installed at the outlet of the combustion chamber.

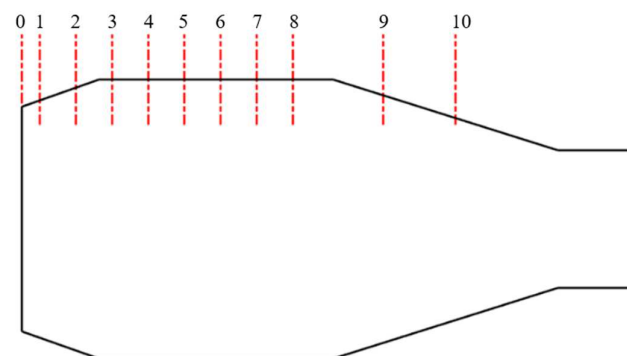


**Figure 6.** Thermocouple and static pressure sensor position.

### 2.4. Experimental Results and Analysis

The experimental test is started from the ignition point and loaded up to full speed no load (FSNL) with an increase in fuel mass flow, air mass flow, air temperature, and pressure, which is the same as the operation of real gas turbine. After reaching FSNL, the test continues with loading up and modulating the fuel split between the central stage and the main premix stage at every 10% relative load.

Figure 7 shows the temperature variation with the load change monitored with thermocouples at different positions of the NPCS burner. It can be noted that T1, located upstream of the chamber close to the burner outlet (seen in Figure 6), exhibits a relatively small variation with load. T3 and T5, positioned in the middle of the chamber, experiences a slight temperature increases during the process of 40% to 45% load due to the increase in the global equivalence ratio, followed by a significant decrease in temperature amounting to nearly 500 K during the process of 45% to 50%, and a gradual rise as the load further increases. At the downstream of the combustion chamber, T7 undergoes a slightly decrease

during the 45% to 50% process, then gradually increases with the further load increase. Meanwhile, T8 shows a gradual increase with the increase of load.

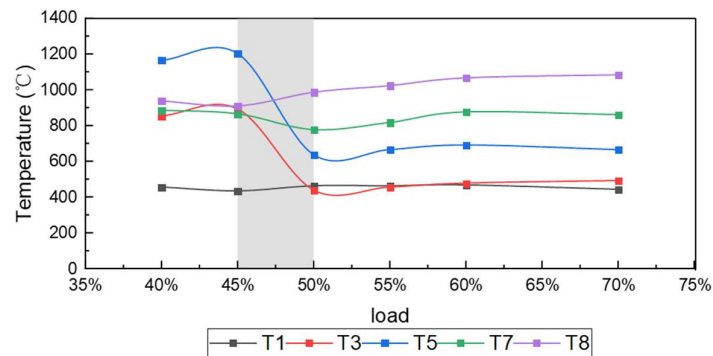


**Figure 7.** The variation in temperature with the loads at different positions for the NPCS burner.

Figure 8 illustrates the variation in differential pressure, with the load measured at different positions.  $\Delta P1$ , positioned upstream of the chamber near the burner inlet, exhibits a relatively small variation with load. In addition, the differential pressures  $\Delta P3$  and  $\Delta P5$ , situated in the middle of the chamber, exhibit nearly constant values during the process of 40% to 45% load. However, in the process of 45% to 50% load,  $\Delta P5$  undergoes a significant decrease, and its value changes from positive to negative, while  $\Delta P3$  significantly increases with the load. At load > 50%, the differential pressures  $\Delta P3$  and  $\Delta P5$  remain stable with the increasing loading. The differential pressures,  $\Delta P7$  and  $\Delta P8$ , situated downstream of the combustion chamber, both exhibit a slight increase with the increase in load.

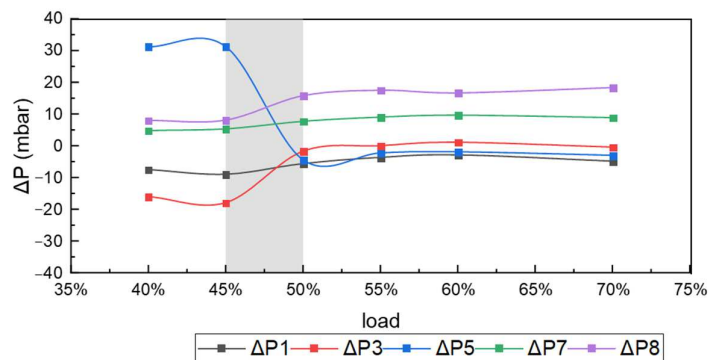


**Figure 8.** The variation in differential pressure with the loads at various positions for the NPCS burner.

It is noteworthy that that T3 and T5, as well as  $\Delta P3$  and  $\Delta P5$ , display great changes during 45% to 50% load, indicating substantial alterations in the combustion chamber. Therefore, the near-wall temperature distribution along the axis was extracted for 45–50% load, as shown in Figure 9. NPCS-before represents the condition at 45% load, and NPCS-after indicates the condition at 50% load. At 45% load, the temperature in the middle of the combustion chamber significantly rises, forming a prominent protrusion. Meanwhile, the temperature decreases significantly from T6 to T7. In general, the temperature distribution shows a pattern of high in the middle and low on both sides along the axis. At 50% load, in the middle of the combustion chamber, the temperature distribution is relatively smooth, and increases in a stepped pattern along the axial direction, while the temperature shows minimal changes along the axial direction downstream of the combustion chamber. This indicates a noticeable change in the flame shape changes, temperature distribution, and differential pressure as the load increases from 45% to 50% load, which signifies a flame transition. For NPCS, the thermocouples measuring showing significant temperature changes before and after the flame transition, which are T3~T6.

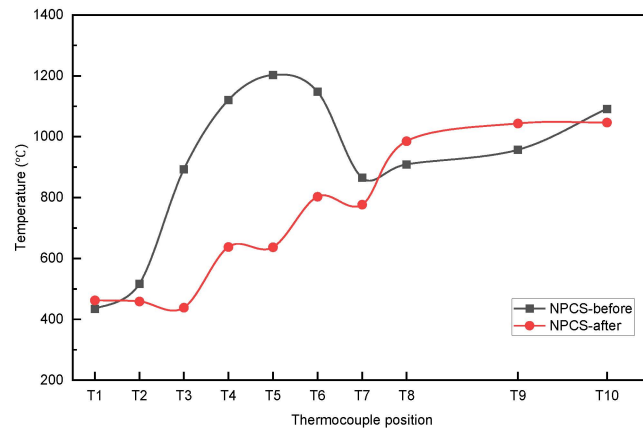


Figure 9. Near-wall temperature distribution of the NPCS burner at 45% and 50% load.

Figure 10 shows the variation in temperature with load monitored by thermocouples at different positions for the PCS burner. At load  $\leq 60\%$ , the temperature monitored by each thermocouple gradually increases as the load rises from 40% to 60%. During the process of 60% to 65% load, temperatures at the midstream of the combustion chamber (T3 and T5) and downstream of the combustion chamber (T7) exhibit a significant decrease (seen in the shadow area of Figure 10). This trend is consistent with the NPCS burner trend, indicating that the PCS burner undergoes a flame transition during the process of 60% to 65% load. Figure 11 shows the variation in differential pressure at different positions of the PCS burner with loads. Notably,  $\Delta P3$  and  $\Delta P5$  show notable changes,  $\Delta P5$  changes from positive to negative, while the absolute value of  $\Delta P3$  markedly decreases, and  $\Delta P7$  experiences a slight decrease.

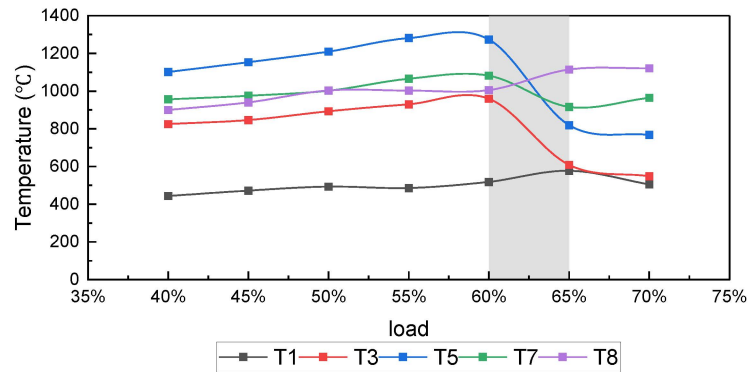


Figure 10. The variation in temperature with the loads at different positions for the PCS burner.

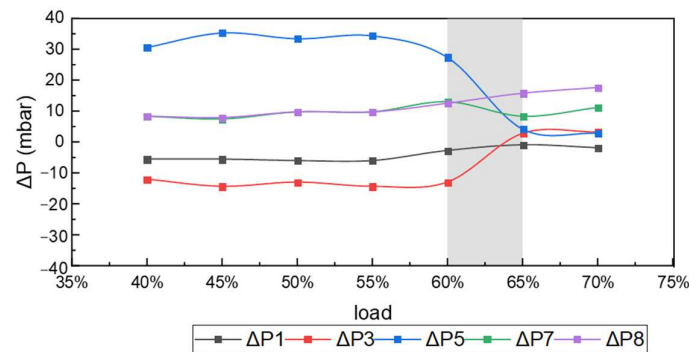


Figure 11. The variation in differential pressure with the load at different positions for the PCS burner.

Figure 12 shows the near-wall temperature distribution along the axis before and after the flame transition for the PCS burner. The distribution pattern of the flame before

and after transition is similar to that of the NPCS burner. Before the flame transition (at 60% load), there is a significant protrusion in the near-wall temperature distribution at the midstream of the combustion chamber (T1–T7), and the near-wall temperature distribution becomes smoother at the downstream of the combustion chamber (T8–T10). After the flame transition (at 65% load), the near-wall temperatures T1–T9 increase gradually along the axial positions, but then the temperature slightly decreases. For the PCS burner, the thermocouples measured indicate significant temperature changes before and after flame transition, which are T3~T7. And compared to the NPCS burner, T7 has a more significant temperature change before and after the flame transition.

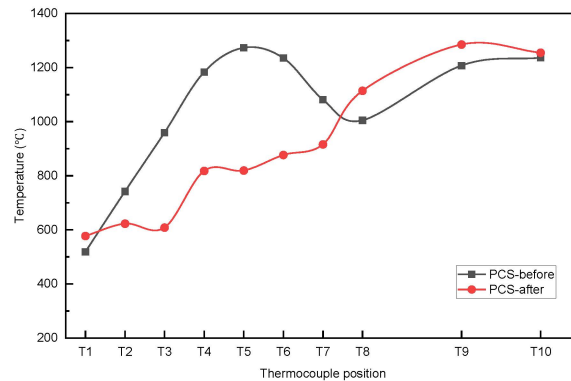


Figure 12. Near-wall temperature distribution before and after the flame transition for the PCS burner.

Figure 13 shows the temperature variation with the load monitored at different positions for the PCSE burner. Especially at loads  $\leq 55\%$ , the temperature monitored by each thermocouple gradually increases as the load increases. During the process of 55% to 60% load, T3 and T5, located in the midstream of the combustion chamber, as well as T7, situated downstream of the combustion chamber, exhibit a significant decrease in temperature, as shown in the shadow area of Figure 13. This suggests that the PCSE burner undergoes a flame transition between 55% and 60% load. Figure 14 shows the variation in differential pressure with the load at different positions for the PCSE burner. It is noteworthy that the differential pressure at different positions showed significant changes.  $\Delta P1$  and  $\Delta P3$  experience a significant decrease as the load increases from 40% to 55%, then rapidly increases as the load rises from 55% to 60%, followed by a minor change as the load changes from 60% to 70%. Specifically,  $\Delta P3$  transitions from negative to positive.  $\Delta P5$  remains relatively stable at loads below 50%, gradually decreasing as the load increases from 50% to 60%, and remaining essentially unchanged after 60% load.  $\Delta P7$  and  $\Delta P8$  exhibit a similar trend to that observed in  $\Delta P1$  and  $\Delta P3$  with load, but with much smaller magnitudes of change.

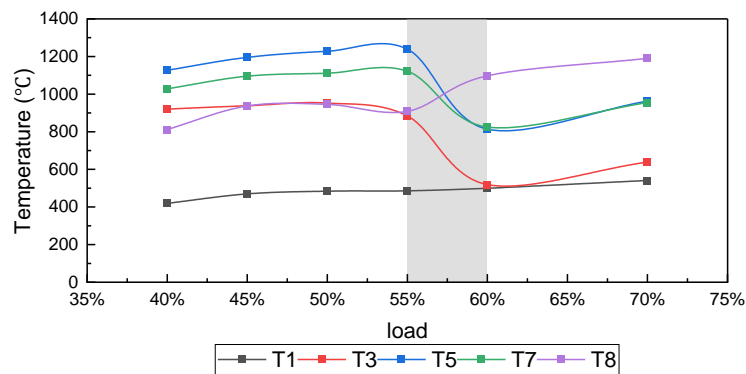
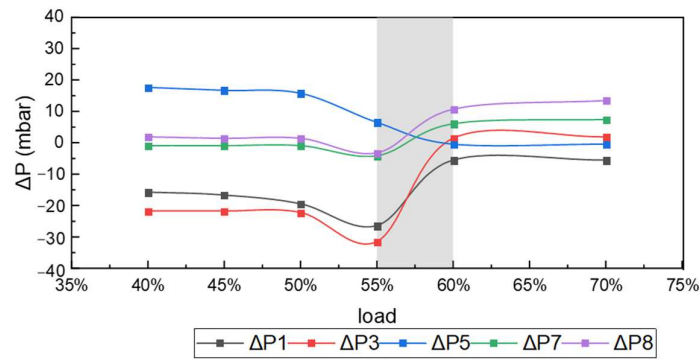
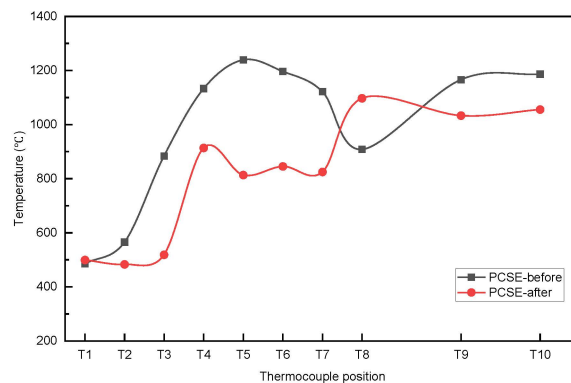


Figure 13. The variation in temperature with the loads at different positions for the PCSE burner.



**Figure 14.** The variation in differential pressure with the load at different positions for the PCSE burner.

Figure 15 shows the near-wall temperature distribution along the axis before and after the flame transition for the PCSE burner. The distribution pattern of its flame before and after transition is similar to that of NPCS and PCS burner. Before the flame transition (at 55% load), a significant protrusion is observed in the near-wall temperature distribution at the midstream of the combustion chamber. And after the flame transition (at 60% load), the near-wall temperature distribution firstly remains unchanged for T1–T3. With the increase in axial position (T3–T5), the temperature rapidly increases and then slightly decreases. In the axial position for T5–T7, there is only a slight variation, and from T7 to T8, there is another rapid increase, with the temperature finally slightly decreasing. For PCSE, the thermocouples with significant temperature changes before and after the flame conversion are T3~T8, and compared to PCS, the influence of the flame conversion on T7 and T8 temperatures is much more pronounced, implying a longer flame for PCSE.



**Figure 15.** Near-wall temperature distribution before and after the flame transition for the PCSE burner.

Figure 16 depicts the influence of central-stage fuel on the NO<sub>x</sub> emission under various loads for the three tested burners; the central-stage fuel quantity is normalized by the total fuel at the design point. Notably, the quantity of the central stage fuel under different loads shown in the Figure represents the value that achieves the lowest NO<sub>x</sub> emissions while maintaining stable combustion. For the load ranging from 45% to 70%, the variations in the quantity of central stage fuel are evident among the three tested burners. As illustrated above, the central-stage combustion mode differs among the three burners. Specifically, the NPCS burner adopts a diffusion combustion mode, resulting in a higher temperature that promotes the formation of NO<sub>x</sub>. Conversely, the central-stage combustion mode of PCS burner is premix combustion. As a result, the mixing quality of the central stage for PCS is significantly enhanced. This improvement results in a reduction of the central-stage flame temperature, thereby contributing to the mitigation of NO<sub>x</sub> emissions. To achieve low NO<sub>x</sub> emission, the central-stage fuel quantity of the NPCS burner is lower than the PCS burner,

with the difference becoming more pronounced at high load (60% to 70%). Conversely, by removing the orifice plate to increase the air mass flow rate of the central stage so as to enhance the mixing quality further, the central-stage fuel is higher than the PCS burner, and the  $\text{NO}_x$  emissions of the PCSE burner are slightly smaller compared to that of PCS.

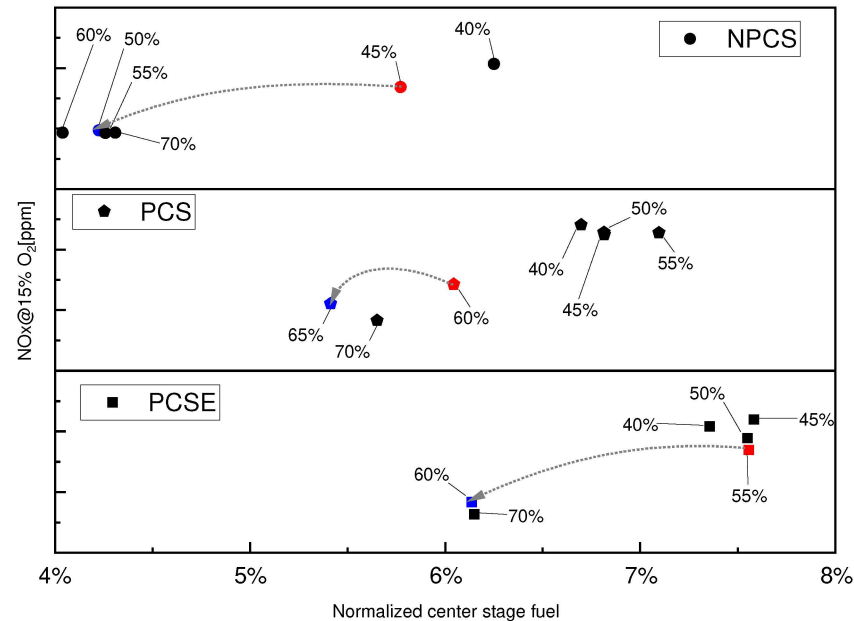


**Figure 16.**  $\text{NO}_x$  emission under various central stage fuel for different burners.

The gray dashed line with the arrow connecting the red point and blue point represents the flame transition process. Here, the red point signifies the load before the flame transition, while the blue point corresponds to the load after the flame transition. Remarkably, the flame transition load for the NPCS burner is much lower than that of the PCS burner. And the alteration in the quantity of central-stage fuel before and after the flame transition is almost 1.5%, significantly exceeding that of the PCS, whose change is approximately 0.6% before and after the flame transition. The flame transition load for the PCSE burner is also lower than the PCS burner, and the change in quantity of central-stage fuel before and after the flame transition is almost 1.4%, exceeding that of the PCS burner. Overall, the  $\text{NO}_x$  emission for the three burners decrease after flame transition.

Based on the full-pressure and full-temperature test, even with the adoption of different combustion modes (diffusion combustion or premix combustion) in the central stage, it was found that there is an abrupt change in near-wall temperature distribution for the three burners when loading up to a certain threshold, indicating a transition in the flame behavior inside the chamber. However, the flame transition load and central-stage fuel quantity differ for each burner. It is crucial to emphasize that, owing to the elevated air pressure, it is difficult to set up a glass window on the combustion chamber. Therefore, capturing the changes in flame morphology through visual measurements in the full temperature and full pressure test becomes challenges. Thereby, numerical simulation methods were used to further analyze the changes in flame morphology during the flame transition for the PCS burner.

### 3. Numerical Simulation

#### 3.1. Simulation Setting

The numerical simulation was performed using the widely used combustion simulation software Fluent 14.0. The polyhedral mesh, with a total mesh number of 8.29 million, was used, and three prismatic layers were added at the fluid–solid interface in order to accurately evaluate the flow near the wall. The computational domain is shown in Figure 17; the types of air inlet boundary condition and fuel inlet boundary condition are the mass

flow inlet, while outlet boundary condition is assigned as the pressure outlet. Both the top and bottom walls are adiabatic with additional cooling air slots, employing mass flow inlets for the cooling air. The side wall adopts periodic boundary conditions. In this study, the interior of the combustion chamber is a strong swirl with shear flow, so the turbulence calculation uses the realizable  $k-\epsilon$  model with scalable wall function. The realizable  $k-\epsilon$  model adds rotation and curvature-related items to the turbulence viscosity calculation, so it can provide superior performance for flows involving rotation and recirculation and ensure the accuracy of the numerical calculation results. The combustion model adopted the partially premixed combustion model and chemical equilibrium models. The Partially Premixed Combustion (PPC) system combines both the concept of a non-premixed model and a pre-mixed model in Ansys Fluent. It solves a transport equation for both the mean reaction progress variable  $C$  (to determine the position of the flame front) and the mean mixture fraction  $f$  (and its variance  $f'$ ). The Chemical Equilibrium model assumes that the species are in a state of dynamic equilibrium and that the details of chemical kinetics are neglected. With the Chemical Equilibrium model, fuel properties are calculated through non-adiabatic equilibrium calculation and they only depend on mean mixture fraction, mixture fraction variance, and enthalpy levels. In this study, the SIMPLE algorithm is used for the coupling of speed and pressure, and the discreteness of the governing equations adopts the second-order precision upwind interpolation format. The boundary condition was consistent with the experiment.

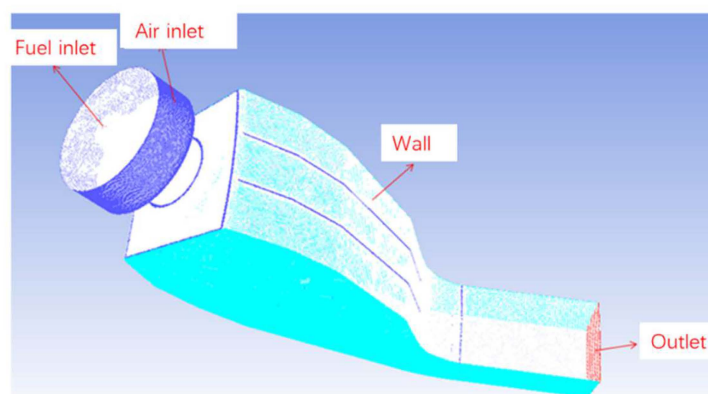


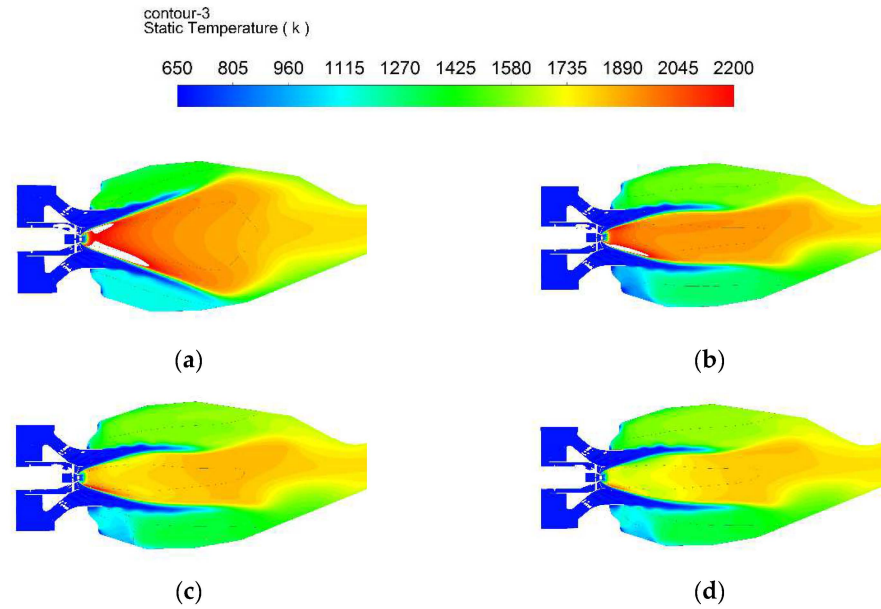
**Figure 17.** Mesh and boundary set up.

### 3.2. Simulated Results and Analysis

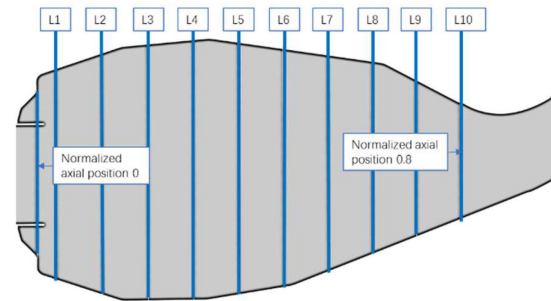
In this study, the effect of the central-stage fuel quantity on the temperature field using the PCS burner was explored. Figure 18 shows the temperature counters of PCS burner under different central-stage fuel quantities in a cross-section plane. Here, CSF means central-stage fuel, which is normalized by the total fuel at the design point. When the CSF decreased from 10% to 8%, a significant change occurs in the temperature distribution. And the flame angle became much smaller, accompanied by a decrease in the temperature within the central recirculation zone. Further decreasing the central-stage fuel, the flame angle remained almost unchanged, while the temperature within the central recirculation zone gradually decreased further.

Figure 19 shows the axial position in the chamber, and the near-wall temperature variation along the chamber axis is shown in Figure 20. When the CSF decreases from 10% to 8%, the near-wall temperature and its distribution trend along the axis show a significant change. At CSF = 10%, the near-wall temperature exhibits a slight decrease as the axial position increases when positions  $\leq 0.3$ . Subsequently, as the axial position rises from 0.3 to 0.6, the near-wall temperature undergoes a rapid increase from 850 °C to 1230 °C. Then, as the axial position continues to increase up to 0.8, the near-wall temperature experiences a gradual rise. At CSF  $\leq 8\%$ , due to the flame transition, the overall distribution trend of the near-wall temperature remains stable; however, significant variations are apparent when compared to the conditions at CSF = 10%. At axial distances  $\leq 0.15$ , the

near-wall temperature exhibits a fluctuating upward pattern due to the influence of the cooling air from the combustion chamber heat shield. At axial distance > 0.15, the near-wall temperature steadily increases with the axial distance. Notably, the near-wall temperature and distribution trend remain almost unchanged as CSF changing from 6% to CSF = 5%, while at CSF = 8%, it is relatively lower than those at CSF = 5–6%.



**Figure 18.** Temperature for different CSFs (blue means low temperature and red means high temperature): (a) CSF = 10%; (b) CSF = 8%; (c) CSF = 6%; (d) CSF = 5%.



**Figure 19.** Line axial position and reference 0 position in chamber.

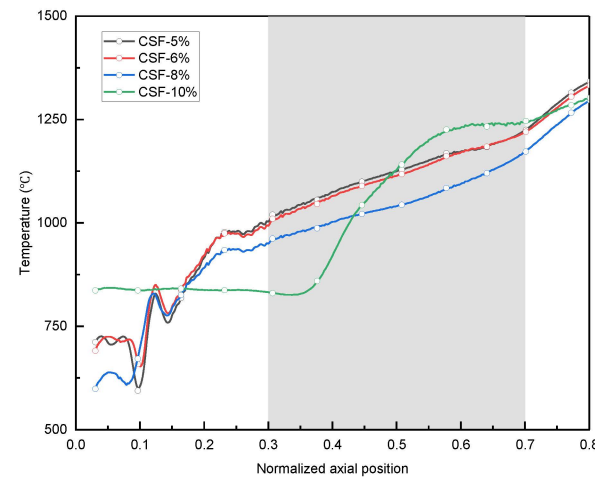


**Figure 20.** Near-wall temperature variation along the chamber axis.

Figure 21 illustrates the distribution of differential pressure along the axis of the combustion chamber for the PCS burner under various central-stage fuel quantities; the static pressure in the 0 position (as shown in Figure 19) is the reference value for calculating the differential pressure, which is consistent with the experimental test. As was similarly observed in the experimental measurement, there was a notable decrease in the differential pressure and its distribution patterns in the midstream of the combustion chamber when CSF decreased from 10% to 8%, which could be attributed to the significant change in the flame shape. At  $CSF \leq 8\%$ , minimal changes are observed in both the differential pressure and its distribution trend, as the flame morphology remains virtually unaltered.

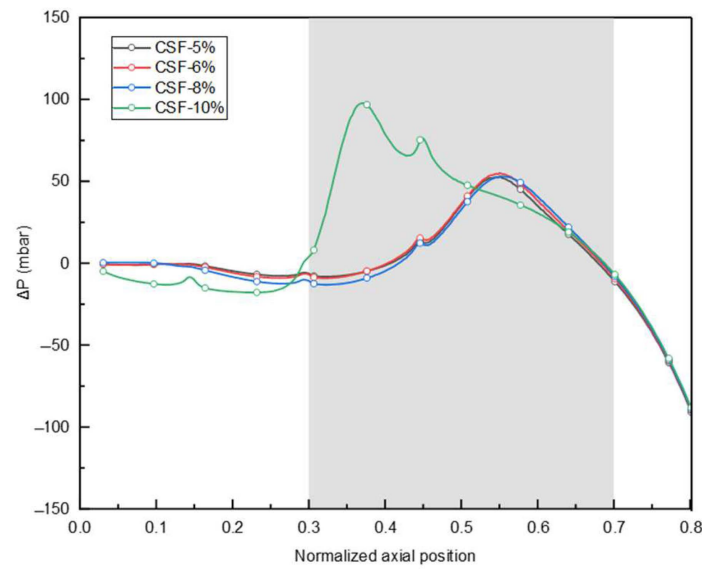


**Figure 21.** Differential pressure distribution along the chamber axis.

Figure 22 shows the radial temperature distribution at different axial positions. At L1 near the burner outlet, both the flame angle and temperature distribution remain consistent for different CSFs, except for a great temperature difference in the central recirculation zone. At L1 near the burner outlet, both the flame angle and temperature distribution remain consistent for different CSFs, except for a great temperature difference in the central recirculation zone. Here, an increase in CSF corresponds to elevated temperatures due to the heightened enrichment of central fuel. In addition, a gradual decrease in CSF results in a reduction in temperature in the central recirculation zone. L2 and L3 are located upstream, where the flame angle begins to differ. While L4~L6 is positioned in the midstream of the combustion chamber, as the CSF decreases from 10% to 8%, there emerges a substantial difference in temperature distribution, with a sharp expansion of the central recirculation zone and a significant increase in temperature in the corner recirculation zone. L8 and L9 are situated near the outlet of the combustion chamber, where the combustion is sufficient, thereby they are less affected by the recirculation zone. The temperature distribution remains consistent under different CSFs. Further decreasing the CSF from 8% results in unchanged temperature distribution at different axial positions, with differences in temperature between the central recirculation zone and the corner recirculation zone.

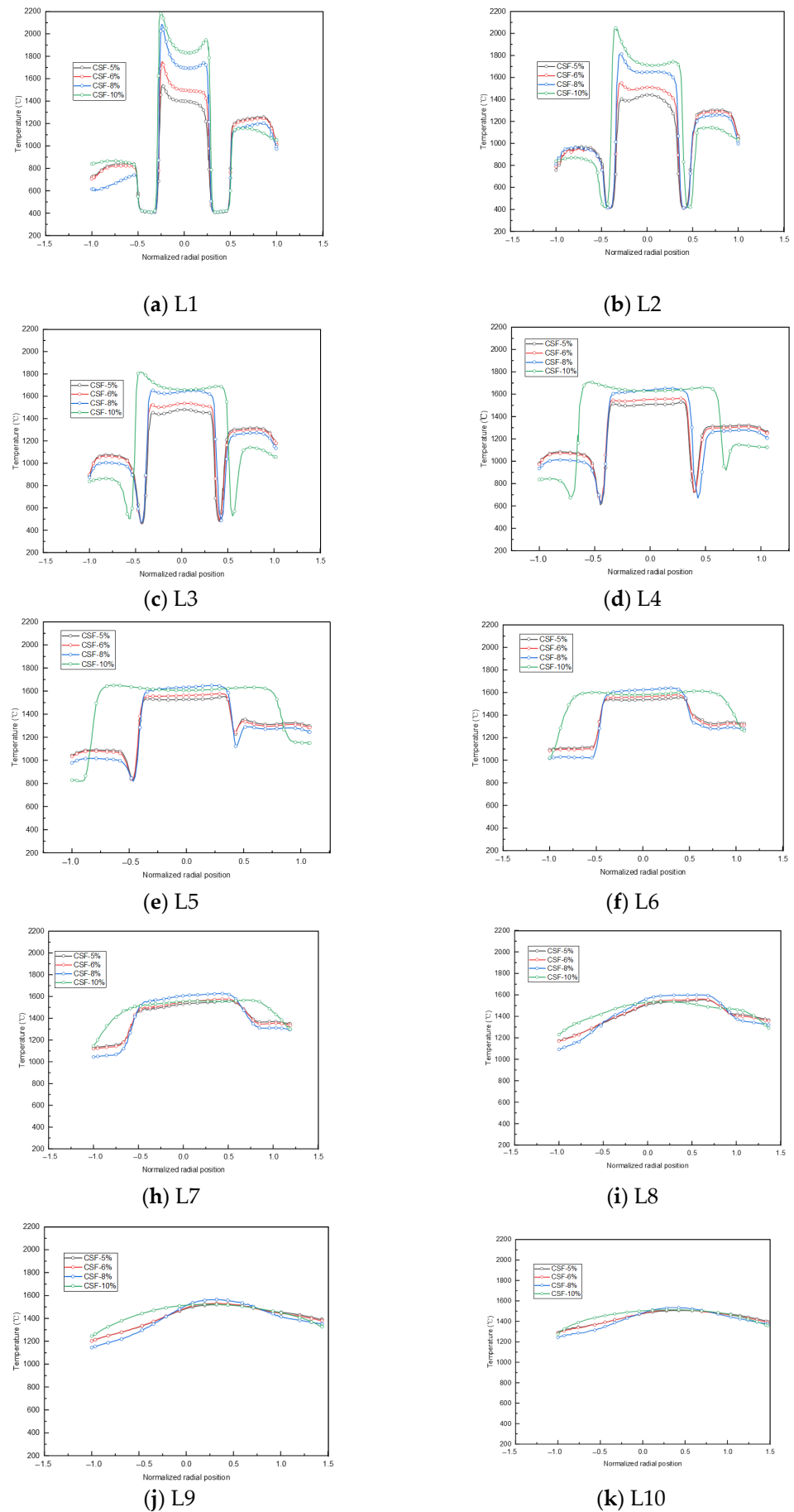


Figure 22. Radial distribution of temperature at different axial positions.

#### 4. Conclusions

This study tested three different burner structures—NPCS burner, PCS burner, and PCSE burner—on a full-temperature, full-pressure, and full-size single burner test bench using both experimental and numerical simulation methods. Two flame shapes were observed in the combustion chamber with variations in gas turbine load and fuel split between the main remix stage and central stage. A transition in flame shape, shifting from an “open” flame to a “closed” flame, occurred during the increase from low load to high load and/or the reduction in the fuel quantity of the central stage. The temperature profiles near the wall and the differential pressure profiles were identified for various flame shapes. The impact laws of the central stage combustion mode and premixing effects on flame transition loads were unveiled: (1) The transition from diffusion to premixing in the central combustion stage results in delayed flame transition loads, occurring as the loading process transitions from the range of 45% to 50% to the range of 60% to 65%. (2) Flame transition loads are comparatively lower in the diffusion central stage, necessitating a reduced amount of fuel. (3) The amplification of premixing effects in the central stage marginally accelerates the flame transition load, shifting it from the range of 60~65% to 55~60%, which concurrently leads to an augmented demand for fuel in the central stage. In numerical analysis, reducing the center stage fuel (CSF = 10% to CSF = 8%) to a certain extent, the near-wall temperature distribution and the radial temperature distribution at different axial positions will undergo significant changes, leading to a sudden change in flame shape. The combustion mode of the central stage and the fuel distribution of the central stage are the main factors affecting the changes in flame shape.

**Author Contributions:** Conceptualization, F.D.; methodology, M.C.; validation, X.H.; investigation, M.Z.; resources, L.Z.; writing—original draft preparation, M.C.; writing—review and editing, L.W. and M.Z.; funding acquisition, H.Z. All authors have read and agreed to the published version of the manuscript.

**Funding:** This research was funded by Heilongjiang Provincial Natural Science Foundation (LH2020E067), the National Science and Technology Major Project (2019-III-0014-0058, J2019-III-0012-0055) and the Hong Kong Scholars Program.

**Data Availability Statement:** The data that support the findings of this study are available from the corresponding author upon reasonable request.

**Conflicts of Interest:** The authors declare no conflicts of interest.

#### References

1. Strantzali, E.; Aravossis, K.; Livanos, G.A. Evaluation of future sustainable electricity generation alternatives: The case of a Greek island. *Renew. Sustain. Energy Rev.* **2017**, *76*, 775–787. [[CrossRef](#)]
2. Lalor, G.; O'Malley, M. Frequency Control on an Island Power System with Increasing Proportions of Combined Cycle Gas Turbines. In Proceedings of the 2003 IEEE Bologna Power Tech Conference, Bologna, Italy, 23–26 June 2003; IEEE: Bologna, Italy, 2003; Volume 4, p. 7.
3. Eulitz, F.; Kuesters, B.; Mildner, F.; Mittelbach, M.; Peters, A.; van den Toorn, B.; Waltke, U.; Rimmington, P.; Wasdell, D. Design and validation of a compressor for a new generation of heavy-duty gas turbines. In Proceedings of the ASME 2007 Power Conference, San Antonio, TX, USA, 17–19 July 2007; pp. 653–663.
4. Vandervort, C. *Advancements in H Class Gas Turbines and Combined Cycle Power Plants*; Turbo Expo: Power for Land, Sea, and Air; American Society of Mechanical Engineers: New York, NY, USA, 2018; p. V003T08A007.
5. Oliveira-Pinto, S.; Rosa-Santos, P.; Taveira-Pinto, F.J.E.C. Management, Electricity supply to offshore oil and gas platforms from renewable ocean wave energy: Overview and case study analysis. *Energy Convers. Manag.* **2019**, *186*, 556–569. [[CrossRef](#)]
6. Bazaluk, O.; Havrysh, V.; Cherednichenko, O.; Nitsenko, V.J.S. Chemically Recuperated Gas Turbines for Offshore Platform: Energy and Environmental Performance. *Sustainability* **2021**, *13*, 12566. [[CrossRef](#)]
7. Lv, X.; Ding, X.; Weng, Y.J.E.P. Performance analysis of island energy system of SOFC and GT with gasified biomass fuel. *Energy Procedia* **2019**, *159*, 406–411. [[CrossRef](#)]
8. Nemitallah, M.A.; Rashwan, S.S.; Mansir, I.B.; Abdelhafez, A.A.; Habib, M.A. Review of novel combustion techniques for clean power production in gas turbines. *Energy Fuels* **2018**, *32*, 979–1004. [[CrossRef](#)]
9. Funke, H.-W.; Beckmann, N.; Abanteriba, S. An overview on dry low NO<sub>x</sub> micromix combustor development for hydrogen-rich gas turbine applications. *Int. J. Hydrogen Energy* **2019**, *44*, 6978–6990. [[CrossRef](#)]

10. Kurata, O.; Iki, N.; Inoue, T.; Matsunuma, T.; Tsujimura, T.; Furutani, H.; Kawano, M.; Arai, K.; Okafor, E.C.; Hayakawa, A. Development of a wide range-operable, rich-lean low-NO<sub>x</sub> combustor for NH<sub>3</sub> fuel gas-turbine power generation. *Proc. Combust. Inst.* **2019**, *37*, 4587–4595. [[CrossRef](#)]
11. Fentaye, A.D.; Baheta, A.T.; Gilani, S.I.; Kyprianidis, K.G. A review on gas turbine gas-path diagnostics: State-of-the-art methods, challenges and opportunities. *Aerospace* **2019**, *6*, 83. [[CrossRef](#)]
12. Stefanizzi, M.; Capurso, T.; Filomeno, G.; Torresi, M.; Pascazio, G. Recent Combustion Strategies in Gas Turbines for Propulsion and Power Generation toward a Zero-Emissions Future: Fuels, Burners, and Combustion Techniques. *Energies* **2021**, *14*, 6694. [[CrossRef](#)]
13. Emami, M.D.; Shahbazian, H.; Sunden, B. Effect of operational parameters on combustion and emissions in an industrial gas turbine combustor. *J. Energy Resour. Technol.* **2019**, *141*, 012202. [[CrossRef](#)]
14. Zeng, G.; Xu, Z.; Zhang, Z.; Bai, H. Natural gas-hydrogen hybrid combustion retrofit method and practice for F-class heavy-duty combustion engines. *Eng. Res. Express* **2023**, *5*, 035061. [[CrossRef](#)]
15. He, F.; Li, Z.; Liu, P.; Ma, L.; Pistikopoulos, E.N. Operation window and part-load performance study of a syngas fired gas turbine. *Appl. Energy* **2012**, *89*, 133–141. [[CrossRef](#)]
16. Anisimov, V.V.; Chiarioni, A.; Rofi, L.; Ozzano, C.; Hermeth, S.; Hannebique, G.; Staffelbach, G.; Poinso, T. *Bi-Stable Flame Behaviour of Heavy Duty Gas Turbine Burner: RANS, LES and Experiment Comparison*; Turbo Expo: Power for Land, Sea, and Air; American Society of Mechanical Engineers: New York, NY, USA, 2015; p. V04AT04A041.
17. Wang, F.; Mi, J.; Li, P. Combustion regimes of a jet diffusion flame in hot co-flow. *Energy Fuels* **2013**, *27*, 3488–3498. [[CrossRef](#)]
18. Liu, Y.; Sun, X.; Sethi, V.; Nalianda, D.; Li, Y.-G.; Wang, L. Review of modern low emissions combustion technologies for aero gas turbine engines. *Prog. Aerosp. Sci.* **2017**, *94*, 12–45. [[CrossRef](#)]
19. Färber, J.; Koch, R.; Bauer, H.-J.; Hase, M.; Krebs, W. Effects of pilot fuel and liner cooling on the flame structure in a full scale swirl-stabilized combustion setup. *Gas Turbines Power* **2010**, *132*, 091501. [[CrossRef](#)]
20. Hermsmeyer, H.; Prade, B.; Gruschka, U.; Schmitz, U.; Hoffmann, S.; Krebs, W. V64. 3A Gas Turbine Natural Gas Burner Development. In Proceedings of the ASME Turbo Expo 2002: Power for Land, Sea, and Air, Amsterdam, The Netherlands, 3–6 June 2002; pp. 689–695.
21. Streb, H.; Prade, B.; Hahner, T.; Hoffmann, S. Advanced burner development for the VX4. 3A gas turbines. In Proceedings of the ASME Turbo Expo 2001: Power for Land, Sea, and Air, New Orleans, LA, USA, 4–7 June 2001; Citeseer: New Orleans, LA, USA, 2001; p. V002T02A044.
22. Prade, B.; Streb, H.; Berenbrink, P.; Schetter, B.; Pyka, G. *Development of an Improved Hybrid Burner: Initial Operating Experience in a Gas Turbine*; American Society of Mechanical Engineers: New York, NY, USA, 1996; Volume 78743.
23. Schildmacher, K.-U.; Koch, R. Experimental investigation of the interaction of unsteady flow with combustion. *J. Eng. Gas Turbines Power* **2005**, *127*, 295–300. [[CrossRef](#)]
24. Huth, M.; Heilos, A. Fuel flexibility in gas turbine systems: Impact on burner design and performance. In *Modern Gas Turbine Systems*; Elsevier: Amsterdam, The Netherlands, 2013; pp. 635–684.
25. Thomas, L.L.; Simons, D.W.; Popovic, P.; Romoser, C.E.; Vandale, D.D.; Citeno, J.V. E-class DLN technology advancements, DLN1+. In Proceedings of the ASME 2011 Turbo Expo: Turbine Technical Conference and Exposition, Vancouver, BC, Canada, 6–10 June 2011; pp. 835–845.
26. Vandervort, C. 9 ppm NO<sub>x</sub>/CO Combustion System for “F” Class Industrial Gas Turbines. *J. Eng. Gas Turbines Power* **2001**, *123*, 317–321. [[CrossRef](#)]
27. Venkataraman, K.; Lewis, S.E.; Natarajan, J.; Thomas, S.R.; Citeno, J.V. F-class DLN technology advancements: DLN2. 6. In Proceedings of the ASME 2011 Turbo Expo: Turbine Technical Conference and Exposition, Vancouver, BC, Canada, 6–10 June 2011; pp. 587–594.
28. Joos, F.; Brunner, P.; Schulte-Werning, B.; Syed, K.; Eroglu, A. *Development of the Sequential Combustion System for the ABB GT24/GT26 Gas Turbine Family*; American Society of Mechanical Engineers: New York, NY, USA, 1996; Volume 78750.
29. Guyot, D.; Tea, G.; Appel, C. Low NO<sub>x</sub> lean premix reheat combustion in Alstom GT24 gas turbines. *J. Eng. Gas Turbines Power* **2016**, *138*, 051503. [[CrossRef](#)]
30. Kappis, W.; Florjancic, S.; Ruedel, U. Alstom gas turbine technology overview: Status 2014. In Proceedings of the ASME Turbo Expo 2015: Turbine Technical Conference and Exposition, Montreal, QC, Canada, 15–19 June 2015; Volume 56673, p. V003T08A010.
31. Stuttaford, P.; Rizkalla, H.; Chen, Y.; Copley, B.; Faucett, T. Extended turndown, fuel flexible gas turbine combustion system. In Proceedings of the ASME Turbo Expo 2010: Power for Land, Sea, and Air, Glasgow, UK, 14–18 June 2010; pp. 483–492.
32. Eroglu, A.; Flohr, P.; Brunner, P.; Hellat, J. Combustor design for low emissions and long lifetime requirements. In Proceedings of the ASME Turbo Expo 2009: Power for Land, Sea, and Air, Orlando, FL, USA, 8–12 June 2009; pp. 435–444.
33. Eroglu, A.; Döbbeling, K.; Joos, F.; Brunner, P. Vortex generators in lean-premix combustion. *J. Eng. Gas Turbines Power* **2001**, *123*, 41–49. [[CrossRef](#)]
34. Hughes, M.J.; Berry, J.D.; Zhao, W.; Crawley, B.; Onyima, T.; Feiz, H.; Paasche, E.; Cretegnny, L.; Hong, S.-H.; Genova, T. DLN Evo Combustion Technology Development for a High-Hydrogen Flexible F-Class Retrofit. In Proceedings of the ASME Turbo Expo 2023: Turbomachinery Technical Conference and Exposition, Boston, MA, USA, 26–30 June 2023; American Society of Mechanical Engineers: New York, NY, USA, 2023; p. V03AT04A040.

35. Karim, H.; Natarajan, J.; Narra, V.; Cai, J.; Rao, S.; Kegley, J.; Citeno, J. Staged combustion system for improved emissions operability and flexibility for 7HA class heavy duty gas turbine engine. In Proceedings of the ASME Turbo Expo 2017: Turbomachinery Technical Conference and Exposition, Charlotte, CA, USA, 26–30 June 2017; American Society of Mechanical Engineers: New York, NY, USA, 2017; p. V04AT04A062.
36. Krebs, W.; Schulz, A.; Witzel, B.; Johnson, C.; Laster, W.; Pent, J.; Schilp, R.; Wasif, S.; Weaver, A. Advanced Combustion System for High Efficiency (ACE) of the New SGT5/6-9000HL Gas Turbine. In Proceedings of the ASME Turbo Expo 2022: Turbomachinery Technical Conference and Exposition, Rotterdam, The Netherlands, 13–17 June 2022; American Society of Mechanical Engineers: New York, NY, USA, 2022; p. V03BT04A018.
37. Pennell, D.; Tay-Wo-Chong, L.; Smith, R.; Sierra Sanchez, P.; Ciani, A. GT36 First Stage Development Enabling Load and Fuel (H<sub>2</sub>) Flexibility With Low Emissions. In Proceedings of the ASME Turbo Expo 2023: Turbomachinery Technical Conference and Exposition, Boston, MA, USA, 26–30 June 2023; American Society of Mechanical Engineers: New York, NY, USA, 2023; p. V03BT04A045.
38. Rofi, L.; Anisimov, V.; Chiarioni, A.; Ozzano, C.; Daccà, F. Bi-stable flame behaviour of heavy duty gas turbine burner. In Proceedings of the ASME Turbo Expo 2014: Turbine Technical Conference and Exposition, Düsseldorf, Germany, 16–20 June 2014; American Society of Mechanical Engineers: New York, NY, USA, 2014; p. V04AT04A040.

**Disclaimer/Publisher's Note:** The statements, opinions and data contained in all publications are solely those of the individual author(s) and contributor(s) and not of MDPI and/or the editor(s). MDPI and/or the editor(s) disclaim responsibility for any injury to people or property resulting from any ideas, methods, instructions or products referred to in the content.